



HAL
open science

Mass transport induced by a jet impinging on a density interface: The role of interfacial wave breaking

J. Herault, F. Duval, M. Le Bars

► **To cite this version:**

J. Herault, F. Duval, M. Le Bars. Mass transport induced by a jet impinging on a density interface: The role of interfacial wave breaking. EPL - Europhysics Letters, 2017, 117 (6), 10.1209/0295-5075/117/64003 . hal-01765102

HAL Id: hal-01765102

<https://amu.hal.science/hal-01765102>

Submitted on 8 Jun 2022

HAL is a multi-disciplinary open access archive for the deposit and dissemination of scientific research documents, whether they are published or not. The documents may come from teaching and research institutions in France or abroad, or from public or private research centers.

L'archive ouverte pluridisciplinaire **HAL**, est destinée au dépôt et à la diffusion de documents scientifiques de niveau recherche, publiés ou non, émanant des établissements d'enseignement et de recherche français ou étrangers, des laboratoires publics ou privés.

Mass transport induced by a jet impinging on a density interface: the role of interfacial wave breaking.

J. HERAULT^{1,2}, F. DUVAL¹ and M. LE BARS²

¹ *Institut de Radioprotection et de Sûreté Nucléaire (IRSN), 13115 St Paul lez Durance, France.*

² *Aix Marseille Univ, CNRS, Centrale Marseille, IRPHE, Marseille, France*

PACS 47.27.T – Turbulent transport processes

PACS 47.55.Hd – Stratified flows

Abstract – We report the experimental measurements of mass transport induced by a jet impinging a density interface. Using water/salt-water laboratory experiments, we investigate the mechanism of mass entrainment by performing simultaneous velocity and density measurements. We observe that the mass transport leading to the homogenisation of the density is due to the contribution of the mean fields whereas the turbulent mass flux acts against the entrainment mechanism. Moreover, the turbulent mass flux is almost perpendicular to the density gradient in the impinged region, in contradiction with the classical eddy turbulent diffusion model. We interpret all these features in the framework of interfacial waves breaking. We show how the waves generate a mean flow leading to an enhancement of the entrainment process, and how the turbulent mass flux is correlated to the wave breaking. Finally, we discuss the relevance of the closure schemes used in numerical models (e.g. Reynolds Averaged Navier-Stokes (RANS) equations) to simulate this process.

Introduction. – Turbulent mixing in stratified fluids is one of the challenging problems in fluid mechanics, with key applications in astrophysics, geophysics and in the industry [1, 2]. We consider a situation where two layers of fluids with different density are superimposed so that the initial configuration is stable. The configuration of flows parallel to the interface has been widely studied experimentally and numerically as a canonical framework of stratified mixing [3]. However in many situations, the flow may be non-parallel with a velocity component normal to the interface [4]. In convective stars, thermal plumes impinging the stable stratified radiative region induce a local mixing allowing elements to be transported inside the star [5]. In Earth’s atmosphere, penetrative convection coming from the troposphere is responsible for mixing and internal wave emission into the stratosphere [6]. Mixing by a turbulent jet is also of great interest for nuclear safety studies [7–9]. During the course of a severe accident in a nuclear reactor, hydrogen may be released leading to a stable hydrogen-rich mixture layer in the upper part of the containment. Flammability limits in the hydrogen-rich layer may be reached, which could lead to a deflagration or a detonation. The recent Fukushima accident has questioned the efficiency of the counter-measures to pre-

vent the hydrogen hazard. In the context of nuclear safety, benchmarks between numerical codes and a large scale experiment (8 m in height) of a jet impinging a helium-air interface have been performed [8, 9]. They have pointed out that the first order Reynolds Averaged Navier-Stokes (RANS) models, like the $k - \epsilon$ model, underestimate the entrainment rate [9], questioning the relevance of the eddy diffusivity models. Consequently, the understanding of the mixing mechanisms of a jet impinging a density interface and the measurement of the turbulent flux are of prime interest.

The entrainment transport at a density interface by a turbulent jet has been investigated experimentally [10–13], mostly to characterize the entrainment rate. Guided by qualitative observations [11, 12], the model of entrainment is commonly based on the presence of baroclinic turbulence generated in the impinged region [14]. In contrast, our recent experimental study [15] supports an entrainment driven by interfacial waves, for regimes with moderate deformation of the interface and moderate Reynolds number of the jet, as expected in [16]. We show that the waves are not related to the baroclinic generation of vorticity [11], since density gradients vanish rapidly on both sides of the thin interface [15]. The remaining question

is how the interface perturbations transport mass out of the impinged region. The development of optical measurements allows for the simultaneous measurements of the density and velocity fields, in order to calculate the turbulent mass transport via the cross-correlations of the density and velocity fluctuations. Recent studies of gravity currents have shown that the turbulent mass transport is well described by the Prandtl mixing length model [17,18]. These works have shown that the validation of an eddy diffusivity model for a given configuration can be achieved via measurements of the turbulent mass transport. In this letter, we want to extend this approach to the impinging jet configuration.

We aim to understand the underlying mechanism of mass entrainment by a jet impinging a density interface. We investigate experimentally the mass entrainment via simultaneous density and velocity measurements. Our main result concerns the behaviour of the turbulent mass transport, which acts against the net mass flux and is almost orthogonal to the mean density gradient in the impinged region. We discuss all these features in the framework of interfacial wave propagation. Finally, we question the relevant closure models for the numerical simulations.

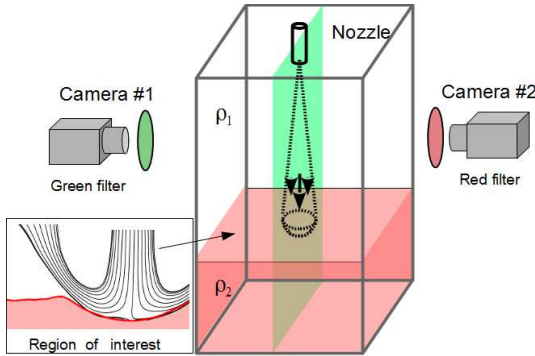


Fig. 1: Sketch of the experimental device.

Set-up. – The set-up is sketched in Fig. 1. The tank is rectangular with a square section of width $L = 30$ cm and height $H = 50$ cm. The tank is filled with one layer of light fluid of density ρ_1 (water+ethanol) and height $h_1 = 26$ cm above a layer of heavy fluid of density ρ_2 (water+salt) and height $h_2 = 17$ cm. The density difference is defined by $\Delta\rho = \rho_2 - \rho_1$. The solution of water plus ethanol allows for the matching of the optical index of the saline solution below. The velocity of injection $U_{in,j}$ at the round nozzle of diameter $d_0 = 0.4$ cm is fixed for each run. The pump for the injection is located in one of the upper corner of the tank. The light fluid pumped inside the tank is then injected through the nozzle: the experiments are thus performed with a constant volume. At the end of each run, the salt water is completely mixed with the upper layer of water plus ethanol. The mixing process is non-stationary: the interface separating both layers is

going down with a typical vertical entrainment velocity $w_e = 85 \mu\text{m/s}$. However, this process is slow relatively to the dynamics of the interfacial waves (period of 2.5 s). We calculate the mean fields during a duration (50 s) large compared to the time-scale of the waves but small compared to the full entrainment process ($2 \cdot 10^4$ s). During 50 s, the net evolution of the density in the upper layer corresponds to 1.5% of $\Delta\rho$. Thus, we expect that the filling box process does not influence the entrainment mechanism during the measurement. The mean fields reported in the letter are computed in the laboratory reference frame. We have compared these results with the mean fields computed in the moving reference frame following the mean interface, with a vertical velocity w_e . The obtained fields are similar with relative variations smaller than 10% .

The velocity and the density fields are measured with two cameras (Grasshopper 3 from PointGrey), respectively indexed 1 and 2 (Fig. 1). The dimensions of the interrogation window are $9.4 \text{ cm} \times 15.6 \text{ cm}$ and both cameras film the same area with a resolution of 600×960 pixels. This region of interest corresponds to half of the impinged region of the interface, illustrated in Fig. 1 (lower left corner), where the streamlines of the mean flow are represented. The vertical laser sheet, generated by a continuous green laser (532 nm), contains the vertical axis of the jet. The flow is seeded with tracer particles ($< 10 \mu\text{m}$) in both layers and the saline solution is premixed with a fluorescent dye (Rhodamine B). During the course of an experiment, the temperature variations are small ($< 1 \text{ K}$) and the fluorescence is not significantly influenced by these effects.

The particles reflect the green light coming from the laser whereas the dye fluoresces in the red (its emission spectrum is $550\text{-}680 \text{ nm}$). The dye concentration in the heavy fluid is $c_0 = 0.012 \text{ mg/L}$: it is low enough so that the fluorescence light response is linear with the dye concentration. A green filter (TIFFEN Green 1) is mounted on camera 1 for the velocity measurements and a red filter (TIFFEN Orange 21) on camera 2 for the density measurements. The flow field is reconstructed using the Particle Image Velocimetry (PIV) process [19], while the density measurement is determined by Planar Laser Induced Fluorescence (PLIF) technique [20]. The resolution of the PIV velocity field is 0.2 cm . The light intensity field recorded by camera 2 is corrected by its flat-field determined by a pre-calibration process. The intensity being proportional to the dye concentration, we can infer the local density difference $c = c_0(I - I_0)/(I_{max} - I_0)$, with I the measured intensity, I_{max} the intensity associated with the initial concentration in the saline solution and I_0 the black response. The local density is given by $\rho = \rho_1 + \delta\rho$ with the density difference $\delta\rho = \Delta\rho(c/c_0)$. The cameras are synchronized so that camera 1 acquires two snapshots with a time lapse of 10 ms while camera 2 takes one snapshot, with a delay shorter than 7 ms relative to the first snapshot of camera 1. This process is repeated at a low frequency $f_{low} = 10 \text{ Hz}$ during 50 s . From the mean position of the interface given by the iso-density line $\delta\rho/\Delta\rho = 0.5$, we define the frame

of reference (x, z) with $x = 0$ the center of the dome and $z = 0$ the bottom of the dome. The region of interest corresponds to the left half of the dome (negative abscissa), where the jet impinges the density interface (see Fig. 1).

The dimensionless parameters characterizing the system are the Reynolds number $Re = U_{inj}d_0/\nu$, with ν the kinematic viscosity, and the initial Froude number at the interface $Fr_i = u_i/\sqrt{b_i g'}$, with u_i and b_i the velocity and the radius of the jet at the interface and $g' = g\Delta\rho/\rho$ the relative gravity acceleration. Two cases, indexed by C1 and C2, are reported in this letter with the respective dimensionless parameters $Re = 3.1 \times 10^3$ and $Fr_i = 0.5$ for C1, and $Re = 4.6 \times 10^3$ and $Fr_i = 0.63$ for C2. For each case, we performed 4 series of measurements and we always observed the same features presented in this letter. The results from C1 are reported in Fig. 2, 3, 4, and 6 and the ones from C2 in Fig. 5, 7 and 9.

Mass transport across the interface. – Fig. 2(a) shows a snapshot of the density difference obtained by PLIF. The interface is perturbed by interfacial waves, that break in the region $x \in [-3, -5]$ cm. The measured velocity field \mathbf{u} and the density difference field $\delta\rho$ are decomposed using the Reynolds decomposition $\mathbf{u} = \bar{\mathbf{u}} + \mathbf{u}'$ and $\delta\rho = \bar{\delta\rho} + \delta\rho'$, with $\bar{\cdot}$ the time-average operator. Fig. 2(b) shows the fluctuations of the density difference $\delta\rho'$ and velocity fields \mathbf{u}' . The evolution of the density $\bar{\delta\rho}$ is given by the Reynolds-averaged density equation

$$\partial_t (\bar{\delta\rho}) + \nabla \cdot (\Phi + \phi) = 0 \quad (1)$$

with $\Phi = \bar{\mathbf{u}}\bar{\delta\rho}$ and $\phi = \bar{\mathbf{u}'\delta\rho'}$. The sum $\Phi + \phi$ corresponds to the entrained mass flux $\bar{\mathbf{u}}\bar{\delta\rho}$ with Φ and ϕ the respective contributions of the mean fields and the fluctuating fields, also called turbulent flux. The streamlines of the flux Φ (thick black curve) and ϕ (dotted black curve) are shown in Fig. 3. They display two completely different features, since the fluxes are flowing in opposite directions. The streamlines of Φ illustrate the trajectories of salt water patches moving from the heavy to the light fluid. Below the mean interface (white curve corresponding to $\bar{\rho} = 0.5$), the fluid patches are advected toward the dome (increasing abscissa) and passed through the interface. Then, they are entrained outward by the mean flow of the turbulent jet (decreasing abscissa). Finally, the salt water is mixed with the ambient lighter fluid by the turbulent jet. This scenario explains the entrainment mechanism leading to the global mixing process. However, the process is reduced by the contribution of the turbulent flux ϕ , which flows out of the dome. This unexpected behaviour leads to an apparent paradox: the turbulent fluctuations act against the entrainment process. The respective contribution of Φ and ϕ to the net entrainment is quantified by the vectors and the norm of the fields $\Phi + \phi$, Φ and ϕ shown in Fig. 4(a), (b) and (c) respectively. The main contribution comes from the flux Φ : the norm of Φ is at least twice larger than the norm of ϕ in the breaking region and it is significantly larger outside. We observe an enhancement of the

fluxes Φ and ϕ in the region $(x, z) \in [-5, -2] \times [-0.5, 1]$ cm², where the interfacial waves break.

The turbulent flux ϕ displays two striking features: it is almost tangential to the mean position of the interface inside the dome, and it flows from the small to the high density region outside. In contrast to the classical eddy diffusivity model, the flux is perpendicular to the mean density gradient $\nabla\bar{\delta\rho}$ in the impinged region. The vertical component ϕ_z (Fig. 5(a)) and $\partial_z\bar{\delta\rho}$ (Fig. 3) are negative in the breaking region, a behaviour associated with a negative eddy diffusivity.

Role of wave breaking. – The role played by the fluctuations can be understood in the framework of interfacial wave propagation and breaking. Fig. 6 shows the root-mean-square amplitude $A_{rms}(x)$ of the waves, where A is the amplitude perturbation of the interface. The amplitude A_{rms} increases from $x = 0$, where the waves are generated, and reaches the value 0.4 cm for $x \in [-4, -2]$ cm. It corresponds to a large steepness $kA_{rms} \simeq 0.62$ with k the wavenumber associated with the estimated wavelength of 4 cm. The large steepness leads to wave breaking [21], followed by a drop of A_{rms} for $x < -4$ cm. Breaking is believed to be an efficient way that momentum is passed from the wave field into the mean flow [22]. If this mechanism is present, an increase of the mean flow energy must be seen through the action of the Reynolds stress. Fig. 5(b) shows the transfer of energy from the mean flow to the wave, given by $P = -\overline{u'_x u'_z S_0}$ with the shear $S_0 = \partial_x \bar{u}_z + \partial_z \bar{u}_x$ and the Reynolds stress $\overline{u'_x u'_z}$. It is negative for $x \in [-5, -3]$ cm, where the wave steepness is large. Thus, wave breaking is characterized by an energy transfer from the waves to the mean flow. The flux Φ is also significantly enhanced in this region (Fig. 4(b)). The density $\bar{\delta\rho}$ being almost constant near the interface, an amplification of the mean flow $\bar{\mathbf{u}}$, via the action of the Reynolds stress, explains the flux increase in the breaking region. Furthermore, the mean flow below the interface shows that the waves are sufficiently steep to induce a secondary flow in the heavy fluid. Surprisingly, the turbulence contributes to the entrainment through an energy transfer from the disturbances to the mean flow.

Whereas the entrainment transports mass out of the dome, the turbulent flux flows inward with a positive correlation $\overline{u'_x \delta\rho'}$ for negative abscissae. The joint probability $\mathcal{P}(u'_x, \delta\rho')$ is shown in Fig. 7(a). We observe more events with like-sign fluctuations, leading to a symmetry breaking in the horizontal turbulent entrainment. This can be analysed in the interfacial wave framework. We introduce the height perturbation η from the mean interface position $h(x)$ (see Fig. 8). The sign of density perturbations $\delta\rho'$ is determined by the sign of η . When $\eta > 0$ (respectively $\eta < 0$), the heavy (light) fluid is pushed above (below) the interface and the perturbation $\delta\rho'$ is positive (negative) in the region below the crest (above the trough). Fig. 7(b) shows the conditional probability of a density perturbation $\delta\rho'$ knowing the sign of u'_x .

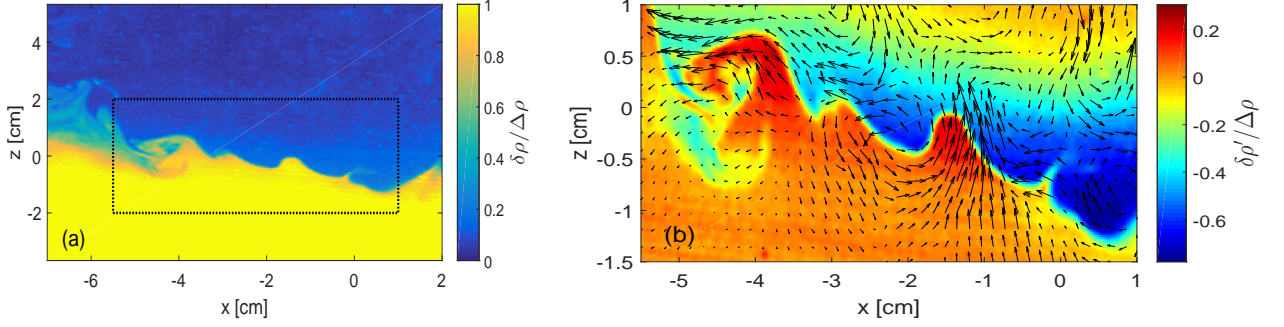


Fig. 2: (a) Relative density snapshot $\delta\rho/\Delta\rho$ (colorplot) obtained from PLIF measurements. (b) Relative density $\delta\rho'/\Delta\rho$ (colorplot) and velocity \mathbf{u}' (vectors) fluctuations corresponding to the window (black dots) on the left figure.

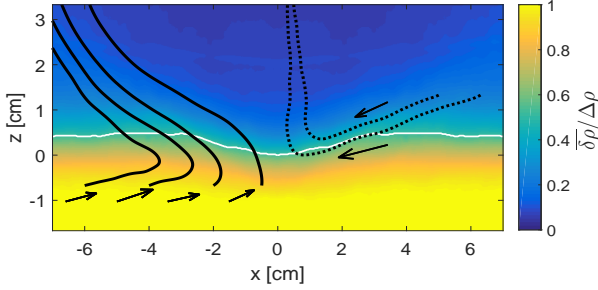


Fig. 3: Streamlines of the fluxes $\Phi = \bar{\mathbf{u}}\bar{\delta\rho}$ (thick black curves) and $\phi = \mathbf{u}'\delta\rho'$ (dotted black curves) superimposed to the time-averaged relative density $\bar{\delta\rho}/\Delta\rho$. The mean interface (white line) corresponds to $\bar{\rho} = 0.5$. The positive abscissae are obtained by symmetry reflection $-x \rightarrow x$.

Both distributions are related by a reflection symmetry: $\mathcal{P}(\delta\rho'|u'_x > 0) \simeq \mathcal{P}(-\delta\rho'|u'_x < 0)$. The distribution tail is heavier when u'_x and $\delta\rho'$ are like-sign. The horizontal component of the mean flow \bar{u}_x being negative, a slowdown of the mean flow is more probable when the heavy fluid is pushed above the interface (Fig. 8) and reciprocally, an acceleration occurs when the light fluid is pushed downward, explaining the horizontal direction of the turbulent flux.

Following the direction of the vertical gradient $\partial_z \bar{\delta\rho}$, the vertical component ϕ_z is negative in the breaking region. Fig. 5 shows that the region of negative flux ϕ_z and negative power P are well correlated spatially, suggesting that ϕ_z varies with P . Fig. 9 shows the values $-\phi_z$ in the breaking region as a function of $-u'_x u'_z S_0 \partial_z \bar{\rho}$ (grey points). For the sake of clarity, we have calculated the averaged values for sub-intervals of width 0.08 (black circles). We clearly observe a correlation between the two quantities and the functional form of the flux ϕ_z follows the linear law $\phi_z = -\kappa P \partial_z \bar{\rho}$ with $\kappa = 0.14 \pm 0.02 \text{ s}^{-2}$.

The origin of this law can be explained in the framework of monochromatic interfacial waves at a density jump (see Fig. 8). Neutral stable waves exchange continuously

their potential energy into kinetic energy and reciprocally, so that the correlation $\overline{u'_z \delta\rho'}$ is zero. In other words, the vertical velocity component and the density perturbation are in quadrature. In contrast, unstable waves should transport mass in the vertical direction, since the vertical velocity at the wave extrema is non zero due to the wave-envelope modulation (grey dashed line in Fig. 8). We will show latter (see equations (3)-(5)) that the decay of the wave amplitude induces an in-phase component of u'_z with $\delta\rho'$, so that $\overline{u'_z \delta\rho'} \neq 0$. Wave shrinking leads to a negative velocity u'_z below the crest where $\delta\rho' > 0$, and a positive velocity above the trough where $\delta\rho' < 0$. Finally, the correlation $\delta\rho' u'_z$ is negative on both sides of the interface.

We now derive a semi-analytical model to quantify this mechanism. We introduce the height perturbation η and the vertical velocity u'_z of our model wave as

$$\begin{pmatrix} \eta \\ u'_z \end{pmatrix} = e^{\sigma t} \begin{pmatrix} A \cos(\psi) \\ \tilde{u}_z(z) \sin(\psi + \theta_z) \end{pmatrix} \quad (2)$$

with $\psi = \omega t - kz$ the wave phase, A the maximal height of the wave, θ_z the phase detuning, and $\tilde{u}_z(z)$ the vertical structure of the vertical flow. The wave is modulated by an exponential function with a decay-rate σ smaller than the frequency ω . This decay corresponds to the relaxation of the system, from a limit cycle (the wave) to a fix point (the unperturbed interface). For the sake of simplicity, we consider only the fields in the vicinity of the mean interface $h(x)$, i.e. $|z - h|/A \ll 1$, so that the function $\tilde{u}_z(z)$ can be considered constant.

The wave perturbation η separates both layers (Fig. 8) and the density $\rho(z)$ is equal to ρ_1 when $z > \eta$ and ρ_2 when $z < \eta$. Thus, the density difference $\delta\rho$ is a step function defined as 0 for $z > \eta$ and $\Delta\rho$ for $z < \eta$. Near $z \simeq h$, the density field $\delta\rho$ is a step-function of period $2\pi/\omega$. The time-averaged density $\bar{\delta\rho}$ is $\Delta\rho/2$ and the associated density perturbation $\delta\rho'$ is equal to $\Delta\rho/2$ when $\eta > 0$ and $-\Delta\rho/2$ when $\eta < 0$. The calculation of the mean density perturbation leads to $\bar{\delta\rho} = (\Delta\rho/\pi) \arccos[(z - h)/A]$, so that the vertical gradient is $\partial_z \bar{\delta\rho} \simeq -\Delta\rho/(A\pi)$ at $z =$

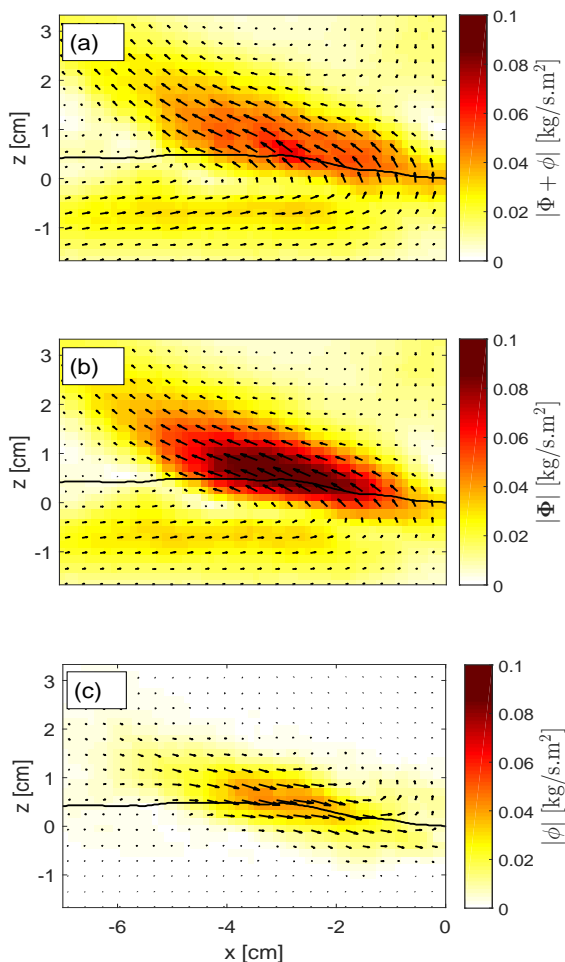


Fig. 4: Net mean density flux $\Phi + \phi = \overline{\mathbf{u}\delta\rho}$ (a), mean flux $\Phi = \overline{\mathbf{u}}\delta\bar{\rho}$ (b), and cross-correlation $\phi = \overline{\mathbf{u}'\delta\rho'}$ (c), expressed in kg/s.m^2 . The vector fields superimposed onto the norm fields correspond to the flux direction. The three figures have the same $x - z$ axis.

h. After averaging over the phase ψ and neglecting the amplitude variation on the time scale σ^{-1} , the correlation between $\delta\rho'$ and u'_z is given by

$$\overline{\delta\rho'u'_z} = \frac{1}{\pi} \tilde{u}_z \sin(\theta_z) \Delta\rho \quad (3)$$

The density difference $\Delta\rho$ can be replaced by $-\pi\partial_z\bar{\rho}$. The relation between u'_z and η is given by the continuity of the material line with $\dot{\eta} = u'_z$. By deriving this equation and separating the odd and even function, we obtain

$$\begin{cases} A\sigma &= \tilde{u}_z(0) \sin(\theta_z) \\ -A\omega &= \tilde{u}_z(0) \cos(\theta_z) \end{cases} \quad (4)$$

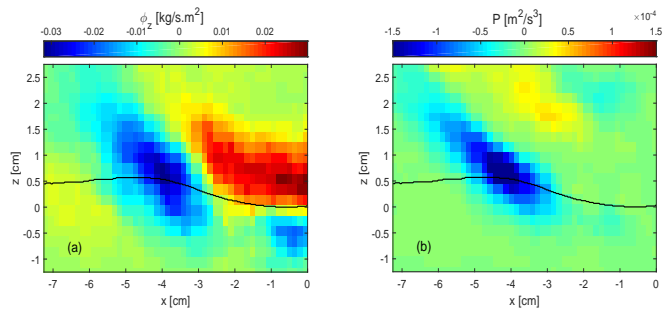


Fig. 5: (a) Vertical turbulent flux $\phi_z = \overline{u'_z\delta\rho'}$. (b) Production term $P = -\overline{u'_z u'_x S_0}$, with $S_0 = \partial_x \bar{u}_z + \partial_z \bar{u}_x$ the shear.

In the limit $|\sigma| \ll \omega$, we get $\theta_z \simeq -\sigma/\omega$ and $\tilde{u}_z(0) \simeq -A\omega$. By substituting the terms, we obtain

$$\overline{\delta\rho'u'_z} = -\sigma A^2 \partial_z \bar{\rho} \quad (5)$$

We estimate the decay-rate with a heuristic model and we derive an energy budget for the interfacial wave at a density jump. The total energy e_t is the sum of the kinetic energy e_c and the potential energy e_p . We now assume the equipartition of energy between the kinetic and potential components, an assumption usually valid for small amplitude waves [22]. Then, the total energy is given by $e_t = \frac{1}{2}\omega^2 A^2 e^{2\sigma t}$. We neglect dissipation and assume that the only energy source-sink comes from the background shear S_0 . The total wave energy equation [23] can be approximated by

$$\frac{de_t}{dt} = -\overline{u'_x u'_z S_0} e^{2\sigma t}. \quad (6)$$

The decay-rate is then given by $\sigma \simeq P/(\omega^2 A^2)$, as also expected from dimensional analysis. Finally, we obtain

$$\overline{\delta\rho'u'_z} = -\frac{1}{\omega^2} (-\overline{u'_x u'_z S_0}) \partial_z \bar{\rho} \quad (7)$$

The value of the pre-factor $\omega^{-2} = 0.16 \pm 0.08 \text{ s}^{-2}$, calculated from the wave frequency, is comparable to the measured one ($\kappa = 0.14 \text{ s}^{-2}$). From this simplified model, we recover the experimental laws. A more complex model should be developed in the Lagrangian reference frame and it should take into account the inhomogeneity of the flow, the diffusive and dissipative effects, and the physics of the breaking. These effects may change the value of the pre-factor. However, we think that the basic physical mechanism is well captured by our simple model.

Conclusion and discussion. – In this letter, we have measured the mass transport associated with the entrainment by a turbulent jet impinging on a density interface. The properties of the entrainment are well described

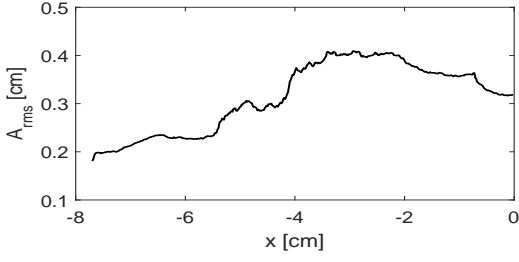


Fig. 6: Root-mean square amplitude A_{rms} of the interface height perturbation in the frequency range $f = 0.4 \pm 0.1$ Hz as a function of x .

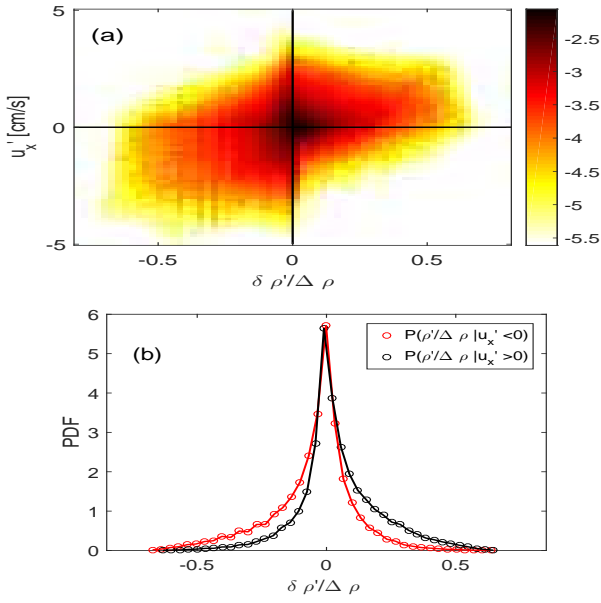


Fig. 7: (a) Joint probability $\mathcal{P}(u'_x, \delta\rho')$ in log scale. (b) Conditional probability $\mathcal{P}(\delta\rho'|u'_x > 0)$ and $\mathcal{P}(\delta\rho'|u'_x < 0)$.

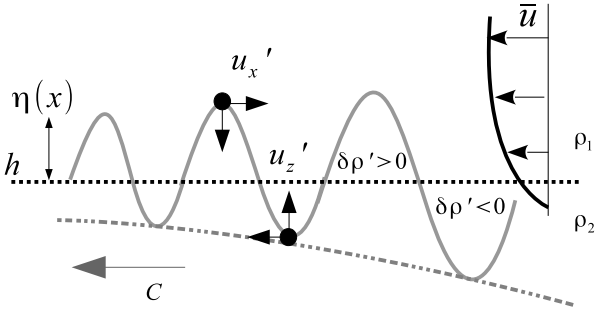


Fig. 8: Schematic illustration of the correlation between the velocity field \mathbf{u}' and density fluctuation $\delta\rho'$. The wave propagates from right to left. The dotted black line is the mean interface position and the dashed grey line is the interface perturbation η . The thick grey line illustrates the decrease of the wave envelope.

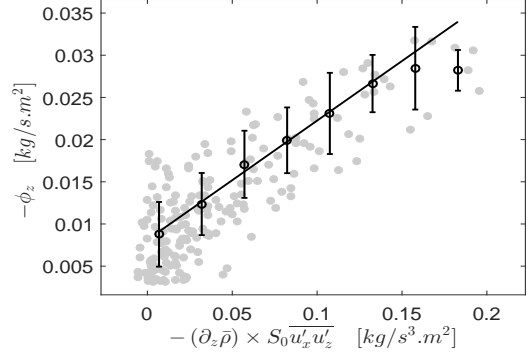


Fig. 9: The opposed vertical turbulent flux $-\phi_z$ as a function of $-\overline{u'_x u'_z} S_0 \partial_z \bar{\rho}$ in the breaking region. The line corresponds to $\phi_z = -0.14 (-\overline{u'_x u'_z} S_0) \partial_z \bar{\rho} + 0.02$

by the breaking of interfacial waves. The total mass transport follows mainly the feature of the flux $\Phi = \bar{\mathbf{u}}\bar{\rho}$, the mass transport due to mean fields, whereas the turbulent flux acts against it. We observe an enhancement of the mean flow by the momentum deposition due to the wave breaking. Our results show that the turbulent mass flux can not be approximated by a classical eddy diffusivity model, because the turbulent flux ϕ is orthogonal to the gradient of the mean density field $\nabla\delta\bar{\rho}$ in the impinged region and the vertical flux ϕ_z and $\partial_z\delta\bar{\rho}$ are like-sign in the breaking region.

Equation (7) is similar to an eddy diffusivity model for the vertical component. The turbulent diffusivity can be negative, depending on the sign of P . In shear-induced instability, the time-averaged power P is positive and we recover the Prandtl model [24] observed in gravity current [17, 18], which states that $\delta\rho' u'_z = -D_t \partial_z \bar{\rho}$ with $D_t = L_\rho^2 |\partial_z \bar{u}_x|$. By associating each term, we obtain $L_\rho^2 = -\overline{u'_x u'_z} / \omega^2$ and $\partial_z \bar{u}_x \simeq S_0$. However, we mentioned previously that our configuration differs from these studies because our results hold for a coherent motion of interfacial waves, so that the regions of amplification ($P > 0$) and breaking ($P < 0$) are distinct.

In the first order RANS model, neither anti-diffusion, nor back scatter are allowed, i.e. the turbulent mass transport ϕ and the energy transfer P must be positive. The failure of this approximation can be explained by the strong anisotropy induced by the sharp density interface. Second order closure models, based on the transport equation for the Reynolds stress $\overline{u'_i u'_j}$ and the turbulent buoyancy flux $\overline{u'_i \rho'}$, are suited for anisotropic flows [25, 26]. This hypothesis has been tested for an impinging jet by comparing the turbulent mass flux between a second order RANS model and a large eddy simulation (LES) [27]. Both simulations reproduce a turbulent mass flux directed toward the center of the impinged region (Fig. 52 in [27]). The main features of the wave breaking seem to be reproduced by the LES simulation [27, 28], whereas the question

is open for RANS models. We suspect that two different physical mechanisms could lead to the same qualitative behaviour. In the RANS simulations, the turbulent flux is more important in the region of strong shear, i.e. above the interface: it is due to the flow inside the upper layer only. On the contrary, in our experiment and in the LES simulations, the turbulent flux is more important in the vicinity of the interface, because it is due to the interfacial waves localised at the density interface. Let us assume that in the strong sheared region, the production term is dominant at leading order in the transport equation for ϕ [25]. The shear term $-\phi_j \partial_j \bar{u}_i$ balances the turbulent production term $-\overline{u'_i u'_j} \partial_j \bar{\rho}$ and we obtain $\phi_j \partial_j \bar{u}_i \simeq -\overline{u'_i u'_j} \partial_j \bar{\rho}$. The vertical gradient being dominant, this balance can be rewritten as

$$\phi_z \simeq \frac{1}{(\partial_z \bar{u}_x)^2} (-\overline{u'_x u'_z} \partial_z \bar{u}_x) \partial_z \bar{\rho} \quad (8)$$

This relation seems very similar to equation (7), but its physical origin completely differs: indeed, the RANS model does not take interfacial waves into account, and mixing mostly comes from the vertical shear induced by the horizontal mean flow above the interface. Accordingly, the typical wave frequency (i.e. the first term on the right-hand side) and the global shear S_0 in (7) are replaced by $\partial_z \bar{u}_x$ in (8). This scenario is supported by the parametric investigation of the control parameter of the RANS simulations [27]. Indeed, a decrease of the buoyancy production does not significantly modify the turbulent flux (coefficient C_{3Y} , Fig. 52 in [27]), showing that it plays a minor role in the RANS model for the turbulent transport, whereas a relative enhancement of the shear term $-\phi_j \partial_j \bar{u}_i$ reduces significantly the turbulent flux from the light to the heavy fluid (coefficient C_{4Y} , Fig. 58 in [27]), as expected by equation (8). This scenario needs to be confirmed by a careful investigation of the RANS simulations but it illustrates how it is possible to generate an anti-diffusive turbulent flux, without taking into account the contribution of the waves. A better agreement between experimental observations and numerical simulations could be achieved at a lower numerical cost by using second order closure model, providing the physics of the waves is respected.

In conclusion, new sets of measurements at larger Reynolds number and for extended ranges of Froude number would be fruitful, respectively to extend the validity of our model for nuclear safety application, and to investigate the universality of our results for other dynamics of the interface.

The authors thank J.-M. Ricaud (IRSN) for stimulating discussions. They acknowledge the support from the Institut de Radioprotection et de Sûreté Nucléaire and from Région PACA (France) under the APEX program 2015 (Project S2URF).

REFERENCES

- [1] FERNANDO H.J.S., *Annu. Rev. Fluid Mech.* **23** , 455-493 (1991)
- [2] IVEY G.N., WINTERS K.B., KOSEFF, J.R., *Annu. Rev. Fluid Mech.* **40**(1) , 169, (2008)
- [3] PELTIER W.R., CAULFIELD C.P., *Annu. Rev. Fluid Mech.* **35**(1) , 135-167 (2003)
- [4] LE BARS M., LECOANET D., PERRARD S., RIBEIRO A., RODET L. , AURNOU J. M., LE GAL P., *Fluid Dyn. Res.* **47**(4) ,045502 (2015)
- [5] CHARBONNEL C., TALON S., *Science* **309**(5744) ,2189-2191 (2005)
- [6] FRITTS D. C, ALEXANDER M J., *Rev. of geophys.* **41**(1) (2003)
- [7] STUDER E., BRINSTER J., TKATSCHENKO I., MIGNOT G., PALADINO D., ANDREANI M., *Nuclear Engineering and Design* **253** , 406-412 (2014)
- [8] KAPULLA R., MIGNOT G., PARANJAPE S., RYAN L., AND PALADINO D. , *Science and Technology of Nuclear Installations* **2014** (2014)
- [9] ANDREANI M., BADILLO, A., KAPULLA R., *Nuclear Engineering and Design* **299** ,59-80 (2016)
- [10] BAINES W. D. , *J. Fluid Mech.* **68**(02) , 309-320 (1975)
- [11] SHY S. S., *Experimental Thermal and Fluid Science* **10**(3) , 355-369 (1995)
- [12] COTEL A. J., GJESTVANG J. A., RAMKHELAWAN N. N., BREIDENTHAL R. E., *Exp. in Fluids* **23**(2) , 155-160 (1997)
- [13] LIN, Y.J.P., LINDEN, P. F, *J. Fluid Mech.* **542** ,2552 (2005)
- [14] SHRINIVAS A. B., HUNT G. R., *J. Fluid Mech.* **757** , 573-598, (2014)
- [15] HERAULT J., FACCHINI G., LE BARS M. , under revision for *J. Fluid Mech.*
- [16] BURRIDGE, H.C. AND HUNT, G.R. , *J. Fluid Mech.* **790** , 407-418, (2016)
- [17] ODIER P., CHEN J., RIVERA M. K., ECKE R. E., *Phys. Rev. Letters* **102**(13) ,134504 (2009)
- [18] ODIER P., CHEN J., ECKE R. E., *Phys. D* **241**(3) ,260-268 (2012)
- [19] MEUNIER P., LEWEKE T., *Exp. in Fluids* **35**(5),408421, (2003)
- [20] CRIMALDI, J. P., *Exp. in Fluids* **44**(6) ,851-863 (2008)
- [21] BABANIN, A., *Breaking and dissipation of ocean surface waves* (2011)
- [22] SUTHERLAND, B., *Internal Gravity Waves.* (2010)
- [23] YOUNG, W. R., WOLFE , C. L., *J. Fluid Mech.* **739** ,276307 (2014)
- [24] PRANDTL L. , *Z. angew. Math. u. Mech.* **5**(3) ,136 (1925)
- [25] RODI W., *J. of Geophys. Res.* **92**(C5) ,5305-5328 (1987)
- [26] UMLAUF L., BURCHARD H., *Cont. Shelf Res.* **25**(7) ,795-827 (2005)
- [27] ZIRKEL A., *Numerical investigation of the turbulence mass transport during the mixing of a stable stratification with a free jet* <http://elib.uni-stuttgart.de/handle/11682/1934> (2011)
- [28] ROHRIG R., JAKIRLIC S., TROPEA C., *J. of Turbulence* **5**(3) ,1-22 (2016)